Temporal afterglow between two pulses of repetitively pulsed argon-acetylene plasma

Temporal afterglow between two pulses of repetitively pulsed argon-acetylene plasma: measuring electron and negatively charged species densities

OPEN ACCESS
IOP Publishing
Journal of Physics D: Applied Physics
J. Phys. D: Appl. Phys. **56** (2023) 365204 (10pp)
https://doi.org/10.1088/1361-6463/acdaa9

Temporal afterglow between two pulses of repetitively pulsed argon-acetylene plasma: measuring electron and negatively charged species densities

M Hasani*, T J M Donders and J Beckers

Department of Applied Physics, Eindhoven University of Technology, Eindhoven 5600 MB, The Netherlands

E-mail: m.hasani@tue.nl

Received 9 March 2023, revised 22 May 2023
Accepted for publication 1 June 2023
Published 9 June 2023

Abstract

The temporal afterglow between two pulses of a repetitively pulsed radio-frequency driven low-pressure argon-acetylene plasma is experimentally explored using laser-induced photodetachment combined with microwave cavity resonance spectroscopy. The densities of electrons and negatively charged species, i.e. anions and dust particles, are measured temporally resolved until 1.9 s in the temporal plasma afterglow. Two different plasma-on times are adjusted to investigate the dynamics of anions and dust particles in the afterglow phase. The measurements show that while electrons decay rapidly within the first few milliseconds of the afterglow phase, the negatively charged species reside much longer in the plasma after the plasma is switched off. The electron density decay is measured to be faster for a longer plasma-on time. This effect is attributed to an enhanced recombination rate due to a higher dust particle density and/or size. The density of negatively charged species decays within two different timescales. The first 20 milliseconds of the afterglow is marked with a rapid decay in the negatively charged species density, in contrast with their slow density decay in the second time scale. Moreover, a residual of the negatively charged species densities is detected as long as 1.9 s after extinguishing the plasma.

Keywords: temporal plasma afterglow, dusty plasma, anions, laser-induced photodetachment

(Some figures may appear in colour only in the online journal)

1. Introduction

Dusty or complex plasmas (i.e. low-pressure plasmas containing nano- to micrometer-sized particulates) have become of considerable importance due to their prevalence in various research areas and applications. From a fundamental viewpoint, dusty plasmas are abundantly present in outer space, e.g. in comet tails [1] and in the rings of Saturn [2]. In laboratories on earth, complex plasmas are used as model systems for studying generic phenomena of condensed matter physics and, in that regard, exhibit phenomena such as crystallization [3], melting [4] and turbulence [5].

On the practical side, applications range from the synthesis of polymers [6], nanostructures [7], and functionalized

* Author to whom any correspondence should be addressed.

nanoparticles [8] to contamination control in photolithography [9, 10] and plasma diagnostics [11].

Dust particles are often externally injected into plasma environments, but can also be spontaneously formed when plasmas are ignited in reactive gases such as silane [12], hexamethyldisiloxane [13], methane, and acetylene [14]. In general, the spontaneous formation of dust particles inside an (often radio frequency (RF) driven) low-pressure plasma can be described by several stages and begins with the polymerization stage [15]. Upon ignition of the plasma in a reactive gas mixture—such as in Ar/C_2H_2 as is the case in this work—negative ions (anions) are formed by the reaction of an electron with a monomer acetylene molecule in a process called dissociative electron attachment [16]:

$$C_2H_2 + e^- \rightarrow C_2H^- + H. \quad (1)$$

The primary C_2H^- anions, electrostatically trapped in the central region of the plasma by virtue of the positive potential of the plasma bulk, can trigger a consecutive chain of polymerization reactions when reacting with other monomer molecules to form larger molecules [17]:

$$C_{2n}H^- + C_2H_2 \rightarrow C_{2n+2}H^- + H_2. \quad (2)$$

Here, the initial polymerization of C_2H^- corresponds to $n = 1$. Subsequently, the particle nucleation stage leads to the formation of small clusters with a size of several nanometers. This process is often dominated by reactions between electrically trapped anions in the plasma and neutral molecules or radicals that contribute to cluster growth [18]. In the next step of particle formation, namely coagulation, the growth of larger dust particles results in gaining an increasing and permanent negative charge. Finally, the particle growth culminates in the accretion step whereby the dust particles grow linearly over time [19]; before the particles fall outside the plasma due to domination of ion drag force.

Experimental diagnostic and numerical modelling studies have been conducted to measure the densities of electrons, ions, neutrals, and dust particles, as well as determine the evolution of the charge of dust particles during steady-state and afterglow plasma conditions. Jiménez-Redondo *et al* [20] studied the first stages of polymerization in Ar/C_2H_2 RF plasmas by mass spectroscopy measurements and with a volume-averaged model. In their measurements, the negative ions distributions showed a clear dominance of ethynyl (C_2H^-) and vinylidene (H_2CC^-) anions while anions with higher molecular weights were found to be present with relatively lower densities. Recently, increasing attention has been devoted to a special case of dusty plasma [21]: a dusty afterglow plasma. In general, afterglow plasmas can be divided into temporal plasma afterglow plasmas (i.e. plasmas extinguishing over time) [22], spatial afterglow plasmas [23] (i.e. plasma residues spatially away from the active (powered) plasma region) or combination of the two [24]. The focus of the current work is on the temporal afterglow of a particle forming plasma. In such type of plasma afterglow, the charge of small nanoparticles was already found to vary slowly in the late afterglow, compared to a rapid decrease of particle charge in the initial stages of afterglow, and eventually to become 'frozen' due to very small positive ion and electron densities and currents in the late afterglow [25, 26]. These results are in agreement with the findings of Couëdel *et al* [27], detecting similar particle charge residuals in the late plasma afterglow. The temporal evolution of the electron density in Ar/C_2H_2 RF plasmas has been experimentally explored by microwave interferometry [28] and microwave cavity resonance spectroscopy (MCRS) [29]. Specifically, an initial release of secondary electrons in the very beginning of the afterglow phase was observed [28, 30] and attributed to the detachment of electrons from the dust particles due to the collision of dust particles with ions [30] or metastables and/or to electron generation by metastable-metastable collisions [31].

The afterglow phase becomes of intrinsic importance when a (dusty) plasma is being repetitively and consecutively pulsed, which has a dominant impact on the dynamics of the negative ions and particles once the plasma is extinguished. From an application point of view, nanoparticle collection [32, 33], pulsed plasma etching [34], and nanoparticle contamination control [35] applications can directly benefit from experimental data aiming at grasping this particular phase. Although temporal afterglows of dusty plasmas have been extensively studied using numerical methods [36–38], experimental data showing the temporal evolution of negatively charged species (i.e. anions and dust particles) are scarce. So far, available experiments have been mainly dedicated to studying de-charging and residual charge measurements of injected microparticles [39–41] and very few on in-situ chemically formed nanoparticles.

In this work, the temporal evolution of the densities of electrons and negatively charged species in the afterglow of a repetitively pulsed dust-forming capacitively coupled RF argon-acetylene plasma is experimentally investigated. For this purpose, the previously developed [42] method of laser-induced photodetachment (LIP) combined with MCRS is applied. Investigated specifically are the plasma afterglow decays of primary anions and small clusters that are formed during different plasma-on times prior to the plasma afterglow phase, i.e. 14 ms and 100 ms.

The current article is structured as follows. In section 2, the experimental methods are briefly explained together with an illustration of the experimental setup. Section 3 presents structured time-resolved measurements of the electron and the negatively charged species densities during the afterglow phase of argon-acetylene plasma. Specifically, the effect of the plasma-on time on the electron and negatively charged species decays are discussed. Finally, section 4 outlines the conclusions and summarizes the study.

2. Methods

The experimental setup used and the methods applied for studying the densities of electrons and negatively charged species have already been previously implemented and discussed

[42]. Here, a description is provided that only briefly explains the experimental methods (i.e. laser-induced photodetachment and MCRS) and describes the distinctive features of the experimental setup.

2.1. MCRS and LIP

MCRS is the method that enables the detection of free electrons within a cylindrical cavity with metallic walls. Initially, microwave resonant modes are excited within this cavity, with each mode having its own electric field distribution and resonance frequency. For the used cavity geometries, this resonance frequency is typically in the GHz frequency range. Upon the emergence of free electrons originating from the plasma, the permittivity ϵ of the medium inside the cavity changes. Consequently, the resonance frequency of the excited resonant mode is subject to a shift. The temporal evolution of the electron density inside the cavity volume is determined by tracking the resonance frequency ($f(t)$) of the excited mode and subtracting it from the resonance frequency (f_0) of the empty cavity (i.e. without plasma). Any presence and transient change in the electron density in the plasma, $\overline{n}_e(t)$, is measured time-resolved by

$$\overline{n}_e(t) = \frac{8\pi^2 m_e \epsilon_0 f^2(t)}{e^2} \frac{f(t) - f_0}{f_0}, \tag{3}$$

where m_e and e are the electron mass and electron charge, respectively, and ϵ_0 is the permittivity of free space. Noteworthy is the fact that the obtained electron densities are electric field (of the applied resonant mode) weighted and (cavity) volume averaged. The spatial distribution of the microwave electric field of the used resonant mode, TM_{010}, indicates the regions in which the resonant mode is most sensitive to the presence of free electrons. A 3D simulation of TM_{010} microwave mode is provided previously [42] and is illustrated in figure 2, showing that the central region of the cylindrical cavity is maximally sensitive and decreases radially. As for the cavity used in this research, the internal diameter and height were 170 mm and 67 mm, respectively. The fundamental resonance frequency was $f_0 = 1.3678$ GHz, and the quality factor was $Q = 397$. Therefore the time resolution of the MCRS system limited by the cavity's response time was $\tau = \frac{2Q}{2\pi f_0} = 92$ ns.

While MCRS is an approach for electron density measurement, LIP, combined with MCRS, is an indirect method of detecting negatively charged species. Upon the incidence of laser photons, the electrons may be detached from the negatively charged species (i.e. anions or dust particles) that are subsequently converted to electron-neutral pairs. The necessary condition for photodetachment occurrence is that the photon energy ($h\nu$) exceeds the electron affinity of the negatively charged species. Generally, in the first few milliseconds of the particle formation process, anions first begin to emerge due to the dissociative attachment of electrons to monomer molecules [16, 43]. A list of five species of anions with the most abundance [44], together with their photodetachment threshold energies, is presented in table 1.

Table 1. Electron affinities of negatively charged species [45, 46].

Negative ion	Electron affinity (eV)
$H_2CC^- + h\nu \rightarrow C_2H_2 + e^-$	0.490
$C_2H^- + h\nu \rightarrow C_2H\cdot + e^-$	2.956
$C_4H^- + h\nu \rightarrow C_4H\cdot + e^-$	3.558
$C_6H^- + h\nu \rightarrow C_6H\cdot + e^-$	3.809
$C_8H^- + h\nu \rightarrow C_8H\cdot + e^-$	3.966

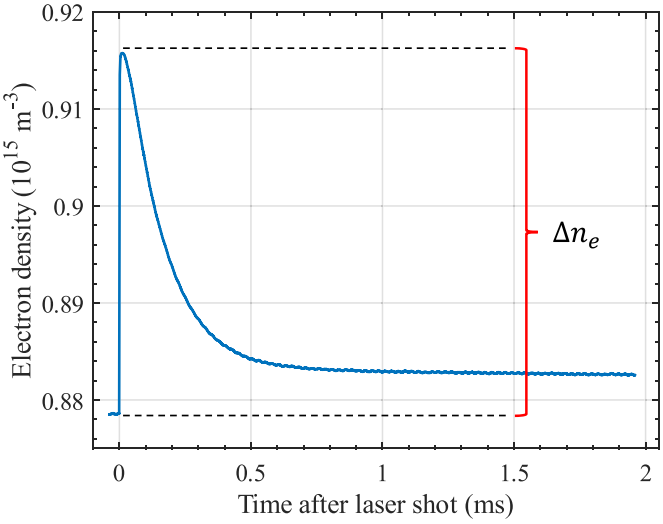

Figure 1. Typical measurement of electron release upon photodetachment incident ($t = 0$): an additional electron density (Δn_e) is detected with MCRS. Here the plasma operates at steady-state conditions of 10 Pa pressure of argon-acetylene gas and 10 W deposited power.

The fourth harmonic of an Nd:YAG laser was chosen to detect the anions and particle charge density for all the photodetachment experiments presented here. The laser light wavelength, therefore, was 266 nm equivalent to a photon energy of 4.66 eV. Consequently, the laser was capable of inducing photodetachment events from all of the anion species mentioned in table 1.

Upon the photodetachment incident, a sudden local surge of electron density is detected, using MCRS, as an additional temporal shift in resonance frequency. As illustrated in figure 1, this photodetachment incident clearly appears as a momentary electron release resolved via equation (3).

Ideally, the laser pulse is capable of converting all of the negatively charged species into electron-neutral pairs. In that case, the diagnostic is operated in its saturation regime. Photodetachment in the saturation regime often demands a high laser pulse energy. In our case, however, the laser pulse only partially converted the negatively charged species along its path. The photodetached electron density, in this case, scales exponentially with the laser pulse energy and photodetachment cross-section of the negatively charged species. The fraction (α) between the photodetached electron density using a specific laser pulse energy (Δn_e) and the photodetached electron density in the saturation regime (Δn_e^{sat}) is given [47] by:

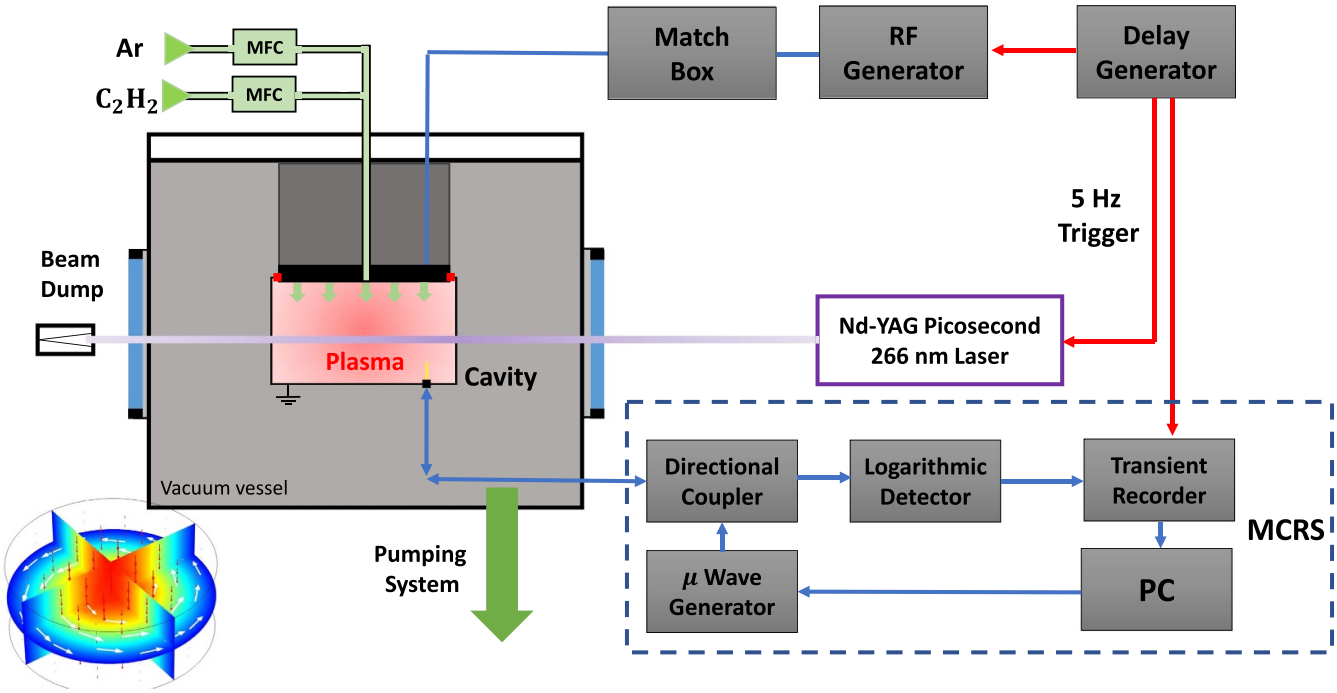

Figure 2. Schematic representation of the experimental setup consisting of three parts: (1). RF plasma generator, used to ignite the plasma inside the cavity in the vacuum vessel. (2). MCRS used to measure electron density. (3). The laser used for photodetachment. The 3D illustration of the spatial distribution of the microwave electric field of TM_{010} in the cavity is also included.

$$\alpha = \frac{\Delta n_e}{\Delta n_e^{\text{sat}}} = 1 - \exp\left(-\frac{\sigma_{\text{det}}}{h\nu}\frac{E_{\text{laser}}}{S}\right), \tag{4}$$

where σ_{det}, $h\nu$, E_{laser}, and S indicate the photodetachment cross section of a specific species, the energy of the photons used for irradiation, the laser pulse energy, and the laser beam's cross-sectional surface area, respectively. In the following experiments, multiple negatively charged species contributed to the overall photodetachment trials. Hence, before performing photodetachment experiments to determine densities of negatively charged species, a preliminary set of experiments is necessary to establish the total cross-section (σ_{det}) and, next, the photodetachment fraction (α).

2.2. Experimental setup

The experimental setup (schematically represented in figure 2), is similar to the setup used for our previous works on photodetachment [42] of oxygen anions in low-pressure plasmas. The experiments were performed in a setup consisting of three main parts: the RF plasma generation base setup, the MCRS diagnostics, and the laser system.

The first part includes all the necessities for generating the asymmetric RF-CCP plasma, i.e. the vacuum vessel, pumps, RF generator, automatic matchbox, and mass flow controllers for feeding argon and acetylene gases at steady flows of 9.1 SCCM and 1.9 SCCM, respectively. The gas pressure was set to 10 Pa by controlling a butterfly valve. The RF generator delivered a 10 W pulsed 13.56 MHz RF signal, which was almost totally absorbed by the plasma during the plasma-on phase. The delay generator set the plasma pulse repetition frequency to 5 Hz for experiments with 14 ms plasma-on time prior to the afterglow phase and 0.5 Hz for experiments with 100 ms plasma-on time prior to the afterglow phase. This pulse repetition frequency was chosen such that the duty cycle was rather low (7% and 5% for experiments with plasma-on times of 14 ms and 100 ms, respectively), i.e. short plasma-on times compared to the duration of the afterglow phases under investigation. The reason for the slight difference (7% versus 5%) in the duty cycle lies in the fact that at least 14 ms plasma-on time was needed in order to obtain reproducible repetitively pulsed discharges and measurements.

The second part includes the equipment for MCRS measurements. The TM_{010} resonant mode was excited within the cavity volume while the shift of its resonance frequency was tracked time-resolved using a transient recorder. The data-acquisition hardware and the data processing are delineated extensively in our previous publication [42].

The pulsed Nd:YAG laser (Ekspla SL235) operated at its fourth-harmonic mode (266 nm wavelength). The laser pulses had a duration of 150 ps and a 5 Hz repetition rate. The beam energy was adjusted to a maximum of 90 mJ per pulse. The delay generator was used to trigger the laser and synchronise the laser pulses with the plasma pulses and MCRS

measurements. The laser was triggered to irradiate during the afterglow phase with adjustable delays compared to the moment when the plasma was switched off.

The detection limit of the current diagnostic method for measuring the density of negatively charged species—via electron release due to photodetachment events—was $10^{12}\,\mathrm{m}^{-3}$. This was determined by the stability of the laser beam energy and the reproducibility of repetitive plasma events. The measurement error stems mainly from a slight instability in the laser beam energy; therefore, the laser beam energy per pulse was measured throughout the experimental campaign. This instability caused a maximum error of 4% in negatively charged species density measurements. Moreover, the error in the electron density measurements was typically 0.1% [42].

3. Results and discussions

The decays of the densities of electrons and negatively charged species (i.e. anions and/or dust particles) during the plasma afterglow were studied by conducting the following experiments. Generally, two sets of experiments were conducted, with each set having had a specific plasma-on time prior to the start of the afterglow phase. The differentiation in plasma-on time was introduced in order to investigate the impact on the afterglow dynamics of anions and/or dust particles. In section 3.1, the decay of the electron density during the afterglow when the plasma was switched on for two different plasma-on times is discussed. Subsequently, in section 3.2, negatively charged species densities measurements and their decays—also for different plasma-on times—are discussed.

3.1. Electron density

The electron density during the afterglow phase was measured time-resolved using MCRS in the TM_{010} mode, probing electrons especially in the central region of the cavity. Figure 3 demonstrates the afterglow behaviour of the electron density when the plasma-on time is subject to change. For a prior plasma-on time of 14 ms, the electron density decayed exponentially with a decay time of $\tau_{\mathrm{loss}} = 447\ \mu\mathrm{s}$ during the afterglow phase. The decay time for the 100 ms plasma-on time case was $\tau'_{\mathrm{loss}} = 352\ \mu\mathrm{s}$, i.e. a 20% shorter decay time compared to the 14 ms plasma-on time case. The decay times mentioned above were obtained by fitting an exponential decay function to the experimentally obtained electron density evolution.

The trend of a faster electron density decay observed for a longer plasma-on time prior to the afterglow phase can be explained by the growth of (more and/or larger) dust particles due to the extended particle formation period. As the particle formation period extends, the initially formed anions may form primary clusters. This effect can—likewise—also be observed from the lower initial electron density just before the afterglow phase for longer plasma-on times (see figure 3); during longer plasma-on times, more electrons are lost by

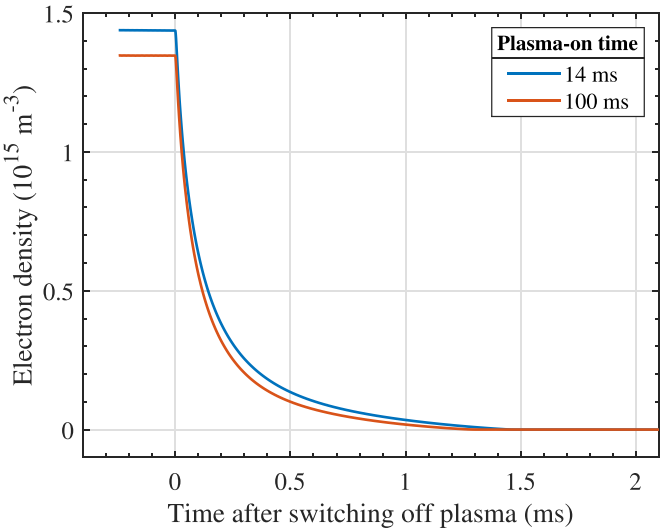

Figure 3. Time-resolved electron densities during the afterglows of 14 ms and 100 ms plasma-on times.

electron attachment [48], to form anions and/or to (growing) dust particles.

Although the lower initial electron density just before the afterglow phase can be explained by an increase in density (and/or size in the case of dust particles) of both anions and dust particles, the fact that for longer plasma-on times the electron density decays faster points to the appearance and/or growth of dust particles in the 100 ms plasma-on time case compared to the situation for the experiments with 14 ms plasma-on time. If the appearance or growth of dust particles had not played a role, longer electron density decay times in the afterglow for longer plasma-on times prior to that afterglow phase would have been expected as, during the afterglow, detachment of electrons from anions would have delayed the overall electron density decay. This hypothetical case is opposite to what is observed.

Overall, from the above, two intermediate conclusions can be drawn. (I) It can be concluded that there are dust particles present in—at least—the afterglows with a prior plasma-on time of 100 ms. Although this could be the case for the 14 ms plasma-on time case as well, it cannot be directly concluded from the available data. (II) It can be concluded that the decay of the electron density in the experiments with 100 ms plasma-on time is dominated by electron loss coupled to the presence of dust particles.

In general, the electron density decay in the afterglow of a dusty plasma is governed by diffusion of plasma species towards plasma-containing walls and recombination onto the dust particles' surfaces [25, 49]:

$$\tau_{\mathrm{loss}}^{-1} = \tau_{\mathrm{diff}}^{-1} + \tau_{\mathrm{recomb}}^{-1}. \tag{5}$$

Here τ_{loss}, τ_{diff}, and τ_{recomb} are decay time scales for the electron density loss, electron diffusion, and recombination losses of electrons due to absorption by dust particles. According to Couëdel *et al* [25], the latter is inversely

proportional to the dust density ($\tau_{\text{recomb}}^{-1} \propto n_d$) when the dust density is low. For the case of high dust density, τ_{recomb} still decreases with dust density. However, the decrease is no longer linear, and the effect of dust particles on the electron loss becomes relatively attenuated. Therefore, an increase in dust particle density enhances surface recombination losses of electrons. As a longer plasma-on time leads to an increased density of dust particles, the electron density can be expected to decay faster due to enhanced recombination rates. Moreover, also larger dust particles formed in extended plasma-on times can contribute to a faster decay rate [25] as $\tau_{\text{loss}}^{-1} \propto r_d^2$.

In order to further support the conclusions drawn above, a third set of measurements is included in appendix. This data set shows the electron density decay in the afterglow phase for a plasma-on time of 1 s. These measurements—in which even larger dust particles were (visibly) present—demonstrate an even further shortened electron density decay time of 147 μs, as is in line with the trend found from the 14 ms and 100 ms plasma-on time cases in this section. Those data are shown in the appendix and not in the main document, as a one-on-one comparison between them and the data presented in this section is questionable as using the 5 Hz laser repetition rate meant that also laser pulses irradiated through the cavity volume during the plasma-on time. Nevertheless, the electron density evolution during the plasma-on time appears reasonably consistent between the three measurements indicating the limited effect of laser irradiation during the plasma-on phase.

3.2. Negatively charged species density

To detect and measure the density of negatively charged species, photodetachment using laser light with a photon energy of 4.66 eV (266 nm wavelength) was applied to the plasma. Here, we define the negatively charged species density as a value connected to the density of the total release of electrons upon a photodetachment experiment. In other words: The total negatively charged species density consists of a contribution from anions and a contribution from electrons released from dust particles. In the latter case, by removing x electrons from each negatively charged dust particle while having a density of n_d, the total contribution from negatively charged dust particles equals xn_d. Upon irradiation of the (former) plasma volume with the laser pulse, the negatively charged species, which had a lower electron affinity than the laser photon energy, yielded an electron release that could be detected using the MCRS technique. Subsequently, equation (4) was used to translate the measured additional electron density (Δn_e), caused by the photodetachment events, to an absolute value of the negatively charged species density (n_-). Initially, it was examined whether the conversion of all the negatively charged species within the laser beam volume (i.e. saturation regime) was achieved. Figure 4 shows the measured values of the photodetached electron density as a function of laser pulse energy. Here, the photodetachment experiments were performed at the end of both plasma-on times of 14 ms and 100 ms, yielding similar results. According to figure 4, the saturation regime could not be fully reached with the laser operating at its maximum energy ($E_{\text{laser}} = 90$ mJ) since the photodetached electron density did not reach a saturated value for that energy yet. Therefore, it was determined what fraction α of the negatively charged species were photodetached by fitting equation (4) to the measured values presented in figure 4, which led to the indirect calculation of the negatively charged species density ($n_- = \frac{\Delta n_e}{\alpha}$) from Δn_e. Just like in basically all preceding LIP experiments [43, 50–52], the value of α was obtained for each prior plasma-on time case once at the beginning of the afterglow phase and was then assumed fixed for the rest of the afterglow. Although this approach appears reasonable during most of the afterglow phase—as the majority of the negative ions is C_2H^-—the value of α might be subject to change towards the end of the afterglow phase when most C_2H^- ions have decayed and the relative contribution of C_2H^- photodetachment to the overall photodetachment signal becomes less dominant. Especially in the very late afterglow phase, future experiments would benefit from a saturation curve measurement (as in figure 4) for each individual measurement point. Although improving the measurement accuracy via the value of α, such an undertaking would increase the overall measurement time—already significantly long—by an order of magnitude. The photodetachment cross-section value, also obtained by the fits for both data sets of 14 ms and 100 ms plasma-on times, was $\sigma_{det} = (6.0 \pm 0.1) \times 10^{-22}\, m^{-2}$, accounting for all the negatively charged species within the laser volume. This value of the photodetachment cross-section is approximately equal to the cross-section value for C_2H^- anion [53, 54]. This implies that a majority of the negatively charged species within the plasma are ethynyl (C_2H^-) anions for both prior plasma-on times, as the other negative ions have different cross-sections. In principle, the same study for the determination of the photodetachment cross-section (σ_{det}) and photodetachment fraction (α) can be performed for longer plasma-on times with larger anions and dust particles.

Referring back to the previous section, it can be concluded that on the one hand, the majority of the species responsible for Δn_e due to photodetachment is C_2H^-, while the decay of the electron density is governed (at least for the 100 ms plasma-on time case) by dust particles.

Subsequently, the total absolute values of the densities of all negatively charged species, including anions mentioned in table 1 and dust particles, were measured time-resolved during the temporal afterglow of the plasma. For this purpose, LIP measurements were performed at a specific and progressing delay time after the plasma was switched off. The repetitively pulsed plasma was driven for more than 100 pulses before the start of LIP measurements, resulting in a steady-state equilibrium of negatively charged species densities after the first plasma pulses. The repetitiveness of the plasma pulses did not lead to the accumulation of negatively charged species over consecutive measurements. Figure 5 illustrates the densities of the negatively charged species together with

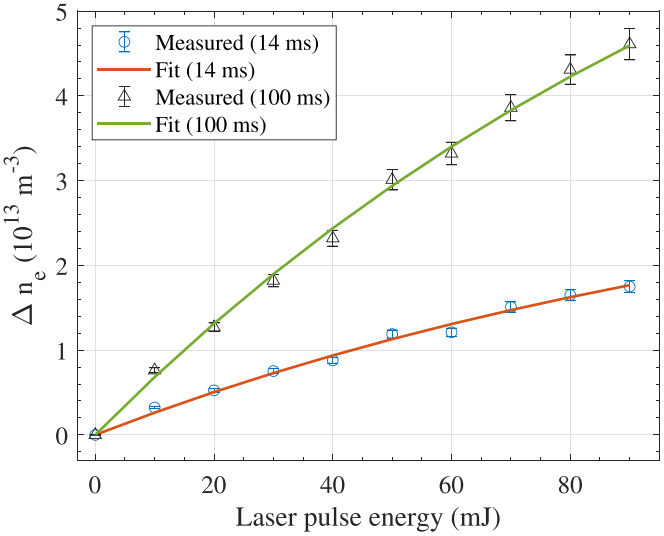

Figure 4. The measured values of photo-detached electron density (Δn_e) as a function of laser pulse energy at the end of 14 ms plasma-on time (blue circles) and 100 ms plasma-on time (black triangles). Equation (4) is fitted with the measured values of 14 ms (red curve) and 100 ms (green curve) plasma-on times.

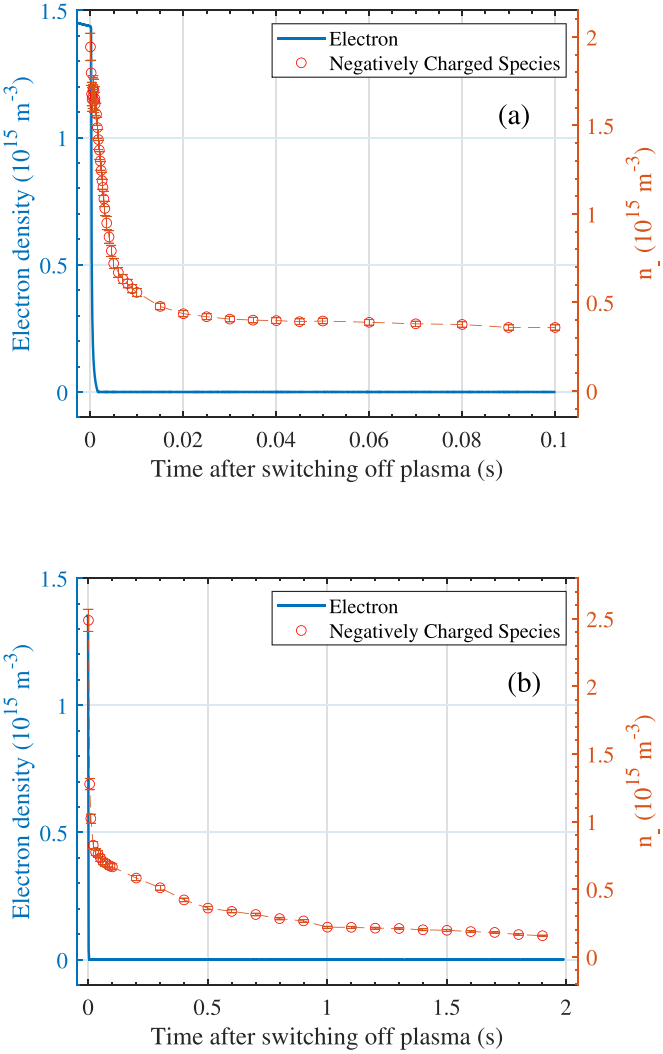

Figure 5. Temporal evolution of electron density (blue curve) together with the density of negatively charged species (n_-, red circles) for plasma-on times of 14 ms (a) and 100 ms (b).

those of the free electrons in the afterglow phase—again—for two different prior plasma-on times of 14 ms and 100 ms (figures 5(a) and (b), respectively). First, in figure 5(a), the argon-acetylene plasma was operated for 14 ms before it was switched off at $t = 0$. As illustrated, the negatively charged species density decayed rapidly by 75% from its initial density of $n_- = (1.94 \pm 0.07) \times 10^{15}\ m^{-3}$ to a density of $n_- = (0.47 \pm 0.01) \times 10^{15}\ m^{-3}$ during the first 15 ms of the afterglow phase. Afterwards, it remained relatively stable during the next 85 ms of the afterglow, as it had decreased to $n_- = (0.35 \pm 0.01) \times 10^{15}\ m^{-3}$ at the final measurement time (100 ms). Subsequently, the plasma-on time was increased to 100 ms. As a consequence of the longer plasma-on time, the negatively charged species density was measured to be relatively higher ($n_- = (2.4 \pm 0.1) \times 10^{15}\ m^{-3}$) at the beginning of the afterglow phase, when compared to that for the experiment with 14 ms plasma-on time. As mentioned earlier, this trend is also indicated by a lower value (for longer plasma-on times) of the electron density prior to the start of the afterglow phase. As seen in figure 5(b), the negatively charged species density decreased by 75% of its initial value to $n_- = (0.58 \pm 0.02) \times 10^{15}\ m^{-3}$ during the first 20 ms of the afterglow phase. Later during the afterglow, the negatively charged species density was measured to slowly decrease to $n_- = (0.15 \pm 0.01) \times 10^{15}\ m^{-3}$ right before the initiation of the next plasma-on phase.

From measurements of the electron and the negatively charged species densities, illustrated in figure 5, it was observed that the negatively charged species decayed following two different timescales while the electrons decayed abruptly at the very early afterglow phase (within the first milliseconds). The initial fast decay of negatively charged species can be explained by, first, the drop in electron temperature (T_e) and, second, the loss of electrons due to diffusion and recombination and, therefore, the ceasing of the quasi-neutrality condition in the plasma.

In general, the beginning of the afterglow is characterized by a sharp decrease in electron temperature [55, 56] resulting in the termination of anion production as well as suppression of the electron current to the dust particles' surfaces. Anions are mainly produced via dissociative attachment of electrons [16]; therefore, when the electron temperature drops from its initial value of typically a few eV to 0.025 eV (room temperature), electrons are no longer capable of producing negative ions. Moreover, as most of the electrons have diffused (mainly by means of ambipolar diffusion, followed by free diffusion) towards the plasma-containing walls or to dust particles' surfaces, the electrostatic confinement of the negatively charged species, i.e. based on the determined photodetachment cross

section in figure 4 dominantly anions, ceases. Therefore an immediate decrease in the density of the negatively charged species is observed in the first 20 milliseconds of the afterglow. Also, suppression of the electron current to the dust particles contributed to the explanation of the swift drop in the density of the negatively charged species. Generally, the charge of dust particles is determined by an equilibrium between the electron and ion currents towards the particles' surfaces [57]. As a result of the electron temperature drop to room temperature and electron losses due to diffusion, the electron current towards the particles is inhibited. In contrast, the ion current stays relatively constant. Therefore, the particle charge becomes less negative due to a relatively higher flux of positive ions towards their surface [26].

In the late afterglow, however, the density of negatively charged species decreased at a much slower rate compared to the early afterglow phase during the first 20 milliseconds. Furthermore, a residual density of negatively charged species was measured in experiments for both plasma-on times. For the case when the plasma-on time was set to 14 ms, negatively charged species residing in the plasma during the entire afterglow is mainly due to a relatively higher plasma pulse repetition frequency (5 Hz). This results in a relatively shorter plasma afterglow time. The observed decay in the afterglow phase can be described by a two-stage mechanism [58]. During the first stage, the electrons diffuse towards chamber walls (and in this case towards dust particles' surfaces) while negative ions are trapped within the plasma, forming a positive-ion-negative-ion plasma, possibly including small dust particles. The second stage in the afterglow begins with diffusing anions and positive ions slowly towards the walls by ion-ion ambipolar diffusion. As simulated previously by Berndt *et al* [59], for sufficiently high repetition frequencies, the anion density only partially decays, and a residual density of anions influences the subsequent plasma pulse in a pulsed RF plasma. In this case, similar to the 14 ms plasma-on time case in figure 5(a), the afterglow time is not long enough for all the anions to diffuse out and the negatively charged species density to decay completely. For the 100 ms plasma-on time (and 0.5 Hz plasma pulse frequency), the slower decreasing trend in the density of negatively charged species can be due to the fact that as nearly all electrons and most negative ions have diffused out, a substantial drop in plasma density prevents any significant change in the charge of dust particles [27]. Therefore, a residual density of negatively charged species (consisting of anions and/or negatively charged dust particles) was observed in both instances of plasma-on times.

4. Conclusions and outlooks

This article presented experimentally obtained results on the temporal afterglows of repetitively pulsed Ar/C_2H_2 plasmas. Electron and negatively charged species densities were measured time-resolved within prolonged afterglows of the plasma up to 1.9 s, using microwave cavity resonance spectroscopy combined with LIP. Two different plasma-on times of 14 ms and 100 ms prior to the start of the afterglow phase were applied to study the contribution of anions and dust particles to the afterglow dynamics. Based on the electron density measurements, it was found that electrons decay faster after longer plasma-on times since the electrons were dominantly lost due to an increased recombination rate as the small (and growing in density and/or size) dust particles acted as additional recombination surfaces. Based on negatively charged species density measurements, it was observed that these densities decay in two stages with different timescales. First, the negatively charged species densities dropped rapidly within the first 20 milliseconds of the afterglow phase. This rapid density drop could be attributed to electron cooling and (ambipolar) diffusion at the very beginning of the afterglow; as the electron temperature and electron density dropped, anions could no longer be formed while they diffuse outwards. Also, the electron current to dust particles may be inhibited by this effect, reducing the number of electrons on dust particles. Second, a much slower decreasing trend was observed in the densities of negatively charged species, resulting from depleted positive-ion-negative-ion plasma density in the late afterglow. Also, for both instances of plasma-on times, a residual density of negatively charged species was detected in the late afterglow.

The research path in this article can be extended to spatio-temporal afterglows of repetitively pulsed dust-forming plasmas. Once the multi-mode microwave resonance spectroscopy [60] is combined with LIP, the evolution of electrons and negatively charged species in different regions of the plasma in a cavity can be studied spatially and temporally resolved.

Data availability statement

All data that support the findings of this study are included within the article (and any supplementary files).

Acknowledgments

The authors acknowledge the financial support of the Dutch Research Council NWO (Project Number 15710) and A B Schrader and P Sanders for their skillful technical support.

Appendix. The afterglow of 1 s plasma-on time

The electron density decay during the plasma afterglow is shown in figure A1. Before extinguishing the plasma, three different plasma-on times, 14 ms, 100 ms, and 1 s, were adjusted to study the effect of plasma-on time on the decay of electron density. As discussed earlier, the plasma-on time of 1 s constitutes a unique case due to the laser irradiation of the plasma during this prolonged plasma-on time. Nonetheless, it can be observed in figure A1 that the electron density decays faster for 1 s plasma-on time ($\tau_{\text{loss}} = 147\ \mu s$), compared to 14 ms and 100 ms plasma-on time cases. Also, a lower initial electron

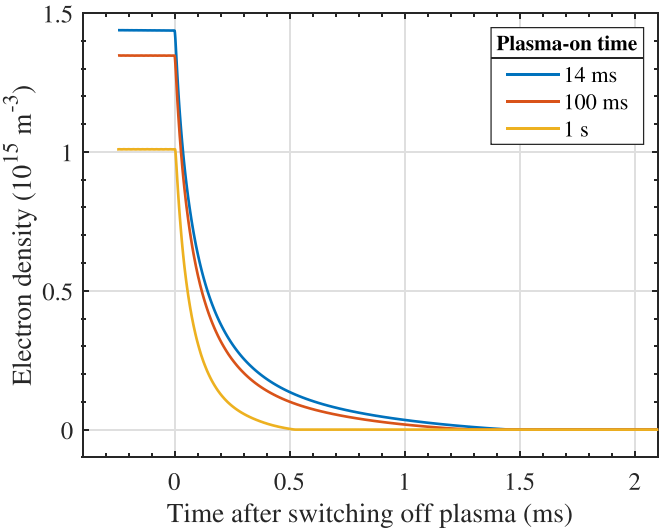

Figure A1. Time-resolved electron densities during the afterglows of 14 ms, 100 ms, and 1 s plasma-on times.

density just before the onset of the afterglow phase is observed for the 1 s plasma-on time.

ORCID iDs

M Hasani https://orcid.org/0000-0001-9227-353X
T J M Donders https://orcid.org/0000-0002-4671-8988
J Beckers https://orcid.org/0000-0001-6116-7013

References

[1] Mamun A A and Shukla P K 2002 Solitary potentials in cometary dusty plasmas *Geophys. Res. Lett.* **29** 17–1–17–4
[2] Wahlund J-E *et al* 2009 Detection of dusty plasma near the E-ring of saturn *Planet. Space Sci.* **57** 1795–806
[3] Thomas H, Morfill G E, Demmel V, Goree J, Feuerbacher B and Möhlmann D 1994 Plasma crystal: coulomb crystallization in a dusty plasma *Phys. Rev. Lett.* **73** 652–5
[4] Nosenko V, Zhdanov S K, Ivlev A V, Knapek C A and Morfill G E 2009 2D melting of plasma crystals: equilibrium and nonequilibrium regimes *Phys. Rev. Lett.* **103** 015001
[5] Zhdanov S, Schwabe M, Räth C, Thomas H M and Morfill G E 2015 Wave turbulence observed in an auto-oscillating complex (dusty) plasma *Europhys. Lett.* **110** 35001
[6] Sciacqua D, von Wahl E, Jagodar A, Pattyn C, Lecas T, Strunskus T, Kovacevic E and Berndt J (Gremi Umr 7344, Cnrs/University Of Orleans and Team Cau Kiel Team) 2020 Towards a better control of plasma polymerization: a case study of plasma produced polyaniline *APS Annual Gaseous Electronics Meeting Abstracts* p YF4–002
[7] Levchenko I, Keidar M, Cvelbar U, Mariotti D, Mai-Prochnow A, Fang J and Ostrikov K K 2016 Novel biomaterials: plasma-enabled nanostructures and functions *J. Phys. D: Appl. Phys.* **49** 273001
[8] Santos M *et al* 2018 Plasma synthesis of carbon-based nanocarriers for linker-free immobilization of bioactive cargo *ACS Appl. Nano Mater.* **1** 580–94
[9] Beckers J, van Minderhout B, Blom P, Kroesen G and Peijnenburg T 2020 Particle contamination control by application of plasma *Proc. SPIE* **11323** 558–63
[10] van de Kerkhof M, Yakunin A, Kvon V, van de Wetering F, Cats S, Heijmans L, Nikipelov A, Lassise A and Banine V 2020 Understanding EUV-induced plasma and application to particle contamination control in EUV scanners *Proc. SPIE* **11323** 239–50
[11] Beckers J, Ockenga T, Wolter M, Stoffels W, Van Dijk J, Kersten H and Kroesen G 2011 Microparticles in a collisional rf plasma sheath under hypergravity conditions as probes for the electric field strength and the particle charge *Phys. Rev. Lett.* **106** 115002
[12] Stoffels E, Stoffels W, Kroesen G and De Hoog F 1996 Dust formation and charging in an Ar/SiH_4 radio-frequency discharge *J. Vac. Sci. Technol.* A **14** 556–61
[13] Donders T, Staps T and Beckers J 2022 Characterization of cyclic dust growth in a low-pressure, radio-frequency driven argon-hexamethyldisiloxane plasma *J. Phys. D: Appl. Phys.* **55** 395203
[14] Winter J, Berndt J, Hong S H, Kovačević E, Stefanović I and Stepanović O 2009 Dust formation in Ar/CH_4 and Ar/C_2H_2 plasmas *Plasma Sources Sci. Technol.* **18** 034010
[15] Bouchoule A 1999 *Dusty Plasmas: Physics, Chemistry and Technological Impact in Plasma Processing* (New York: Wiley)
[16] Stoykov S, Eggs C and Kortshagen U 2001 Plasma chemistry and growth of nanosized particles in a C_2H_2 RF discharge *J. Phys. D: Appl. Phys.* **34** 2160
[17] De Bleecker K, Bogaerts A and Goedheer W 2006 Detailed modeling of hydrocarbon nanoparticle nucleation in acetylene discharges *Phys. Rev.* E **73** 026405
[18] Girshick S L 2020 Particle nucleation and growth in dusty plasmas: on the importance of charged-neutral interactions *J. Vac. Sci. Technol.* A **38** 011001
[19] Boufendi L and Bouchoule A 1994 Particle nucleation and growth in a low-pressure argon-silane discharge *Plasma Sources Sci. Technol.* **3** 262
[20] Jiménez-Redondo M, Tanarro I and Herrero V J 2022 Time evolution of neutral and charged species in Ar/C_2H_2 capacitively-coupled RF discharges *Plasma Sources Sci. Technol.* **31** 065003
[21] Beckers J, Gopalakrishnan R and Goree J 2022 Editorial: particle interaction with afterglow plasma and non-quasi-neutral plasma *Front. Phys.* **10** 1070718
[22] Schweigert I V and Alexandrov A L 2012 Effect of nanoparticles on an rf discharge afterglow *J. Phys. D: Appl. Phys.* **45** 325201
[23] van Minderhout B, van Huijstee J, Rompelberg R, Post A, Peijnenburg A, Blom P and Beckers J 2021 Charge of clustered microparticles measured in spatial plasma afterglows follows the smallest enclosing sphere model *Nat. Commun.* **12** 1–7
[24] van Huijstee J C A, Blom P, Peijnenburg A T A and Beckers J 2022 Spatio-temporal plasma afterglow induces additional neutral drag force on microparticles *Front. Phys.* **10** 926160
[25] Couëdel L, Samarian A, Mikikian M and Boufendi L 2008 Dust density effect on complex plasma decay *Phys. Lett.* A **372** 5336–9
[26] Ivlev A *et al* 2003 Decharging of complex plasmas: first kinetic observations *Phys. Rev. Lett.* **90** 055003
[27] Couëdel L, Mikikian M, Boufendi L and Samarian A A 2006 Residual dust charges in discharge afterglow *Phys. Rev.* E **74** 026403
[28] Berndt J, Kovačević E, Selenin V, Stefanović I and Winter J 2005 Anomalous behaviour of the electron density in a pulsed complex plasma *Plasma Sources Sci. Technol.* **15** 18
[29] Van de Wetering F, Brooimans R, Nijdam S, Beckers J and Kroesen G 2015 Fast and interrupted expansion in cyclic void growth in dusty plasma *J. Phys. D: Appl. Phys.* **48** 035204

[30] Stefanović I, Berndt J, Marić D, Šamara V, Radmilović-Radjenović M, Petrović Z L, Kovačević E and Winter J 2006 Secondary electron emission of carbonaceous dust particles *Phys. Rev.* E **74** 026406
[31] Denysenko I, Stefanović I, Sikimić B, Winter J, Azarenkov N and Sadeghi N 2011 A global model for the afterglow of pure argon and of argon with negatively charged dust particles *J. Phys. D: Appl. Phys.* **44** 205204
[32] Larriba-Andaluz C and Girshick S L 2017 Controlled fluxes of silicon nanoparticles to a substrate in pulsed radio-frequency argon–silane plasmas *Plasma Chem. Plasma Process.* **37** 43–58
[33] Gueye M, Gries T, Noël C, Migot-Choux S, Bulou S, Lecoq E, Choquet P, Kutasi K and Belmonte T 2016 Interaction of (3-aminopropyl) triethoxysilane with pulsed Ar–O_2 afterglow: application to nanoparticles synthesis *Plasma Chem. Plasma Process.* **36** 1031–50
[34] Agarwal A, Rauf S and Collins K 2012 Extraction of negative ions from pulsed electronegative capacitively coupled plasmas *J. Appl. Phys.* **112** 033303
[35] van de Kerkhof M, van Empel T, Lercel M, Smeets C, van de Wetering F, Nikipelov A, Cloin C, Yakunin A and Banine V 2019 Advanced particle contamination control in EUV scanners *Proc. SPIE* **10957** 109570U
[36] Denysenko I, von Wahl E, Labidi S, Mikikian M, Kersten H, Gibert T, E Kovačević and Azarenkov N 2018 Modeling of argon–acetylene dusty plasma *Plasma Phys. Control. Fusion* **61** 014014
[37] Denysenko I, Stefanović I, Sikimić B, Winter J and Azarenkov N 2013 Discharging of dust particles in the afterglow of plasma with large dust density *Phys. Rev.* E **88** 023104
[38] Denysenko I, Stefanović I, Azarenkov N and Burmaka G 2015 Effect of secondary emission on the argon plasma afterglow with large dust density *Phys. Plasmas* **22** 023702
[39] Filatova I, Trukhachev F and Chubrik N 2011 Study of the process of dust grain discharging in the afterglow of an RF discharge *Plasma Phys. Rep.* **37** 1042–5
[40] Wörner L *et al* 2013 The effect of a direct current field on the microparticle charge in the plasma afterglow *Phys. Plasmas* **20** 123702
[41] van Minderhout B, van Huijstee J, Peijnenburg A, Blom P, Kroesen G M and Beckers J 2021 Charge neutralisation of microparticles by pulsing a low-pressure shielded spatial plasma afterglow *Plasma Sources Sci. Technol.* **30** 045016
[42] Hasani M, Marvi Z and Beckers J 2021 Probing negative ions and electrons in the afterglow of a low-pressure oxygen radiofrequency plasma using laser-induced photodetachment *J. Phys. D: Appl. Phys.* **54** 495202
[43] van de Wetering F M J H, Beckers J and Kroesen G M W 2012 Anion dynamics in the first 10 milliseconds of an argon–acetylene radio-frequency plasma *J. Phys. D: Appl. Phys.* **45** 485205
[44] Deschenaux C, Affolter A, Magni D, Hollenstein C and Fayet P 1999 Investigations of CH_4, C_2H_2 and C_2H_4 dusty RF plasmas by means of FTIR absorption spectroscopy and mass spectrometry *J. Phys. D: Appl. Phys.* **32** 1876
[45] Taylor T R, Xu C and Neumark D M 1998 Photoelectron spectra of the $C_{2n}H^-$ (n = 1 − 4) and $C_{2n}D^-$ (n = 1 − 3) anions *J. Chem. Phys.* **108** 10018–26
[46] Lide D R and Haynes W M 2010 *CRC Handbook of Chemistry and Physics* vol 9 (Boca Raton, FL: CRC press)
[47] Bacal M, Hamilton G W, Bruneteau A M, Doucet H J and Taillet J 1979 Measurement of H^- density in plasma by photodetachment *Rev. Sci. Instrum.* **50** 719–21
[48] Stoffels W, Sorokin M and Remy J 2008 Charge and charging of nanoparticles in a SiH_4 rf-plasma *Faraday Discuss.* **137** 115–26
[49] Denysenko I, Stefanović I, Mikikian M, Kovacevic E and Berndt J 2020 Argon/dust and pure argon pulsed plasmas explored using a spatially-averaged model *J. Phys. D: Appl. Phys.* **54** 065202
[50] Vender D, Stoffels W, Stoffels E, Kroesen G and De Hoog F 1995 Charged-species profiles in electronegative radio-frequency plasmas *Phys. Rev.* E **51** 2436
[51] Stoffels E, Stoffels W W, Vender D, Kando M, Kroesen G M W and de Hoog F J 1995 Negative ions in a radio-frequency oxygen plasma *Phys. Rev.* E **51** 2425–35
[52] Haverlag M, Kono A, Passchier D, Kroesen G, Goedheer W and De Hoog F 1991 Measurements of negative ion densities in 13.56-MHz rf plasmas of CF_4, C_2F_6, CHF_3, and C_3F_8 using microwave resonance and the photodetachment effect *J. Appl. Phys.* **70** 3472–80
[53] Best T *et al* 2011 Absolute photodetachment cross-section measurements for hydrocarbon chain anions *Astrophys. J.* **742** 63
[54] Douguet N, Kokoouline V and Orel A E 2014 Photodetachment cross sections of the $C_{2n}H^-(n = 1 - 3)$ hydrocarbon-chain anions *Phys. Rev.* A **90** 063410
[55] Liu F-X, Guo X-M and Pu Y-K 2015 Electron cooling and plasma density decay in early afterglow of low pressure argon plasmas *Plasma Sources Sci. Technol.* **24** 034013
[56] Alexandrov A, Schweigert I and Ariskin D 2013 Kinetic simulations of argon dusty plasma afterglow including metastable atom kinetics *J. Exp. Theor. Phys.* **116** 663–72
[57] Shukla P K and Mamun A 2015 *Introduction to Dusty Plasma Physics* (Boca Raton, FL: CRC press)
[58] Kaganovich I, Ramamurthi B and Economou D J 2001 Spatiotemporal dynamics of charged species in the afterglow of plasmas containing negative ions *Phys. Rev.* E **64** 036402
[59] Berndt J, Kovačević E, Stefanović I and Boufendi L 2009 Controlled dust formation in pulsed rf plasmas *J. Appl. Phys.* **106** 063309
[60] Donders T J M, Staps T J A and Beckers J 2022 Characterization of cyclic dust growth in a low-pressure, radio-frequency driven argon-hexamethyldisiloxane plasma *J. Phys. D: Appl. Phys.* **55** 395203